International Journal of Modern Manufacturing Technologies
ISSN 2067–3604, Vol. XVII, No. 2 / 2025
https://doi.org/ 10.54684/ijmmt.2025.17.2.69

EXPERIMENTAL INVESTIGATION AND FEM ANALYSIS OF HASTELLOY C-22 WELDMENT

Anish K Raj[1], Bikash Ranjan Moharana[2], Kalinga Simant Bal[3], Shaik Mozammil[1]

[1]Department of Mechanical Engineering, C V Raman Global University, Bhubaneswar, Odisha 752054, India
[2]School of Mechanical Engineering, Papua New Guinea University of Technology, Lae-411, Papua New Guinea
[3]Department of Mechanical Engineering, National Institute of Technology, Raipur, Chhattisgarh 492010, India

Corresponding author: Bikash Ranjan Moharana, bikashrnjn@gmail.com

Abstract: Continuous research and innovations to curb the issue of sheet distortion and spattering in electric arc welding of thin sheets (< 2 mm) have led to the inception and development of cold metal transfer and welding (CMWT) at the beginning of the 21st century for joining various materials. A bead-on-plate (BOP) CMTW experiment of SS 308L filler wire on a 1.5-mm-thick Hastelloy C-22 sheet, one of the most commonly used nickel-based superalloy materials in chloride-prevalent environments, has been carried out along with finite element modeling (FEM) of the welding process to predict the thermal history and heat flow distribution. A successfully formed weld bead showed the presence of Fe-rich phases when analyzed through X-ray diffraction (XRD) and energy-dispersive X-ray spectroscopy (EDS), representing effective dissolution of filler wire into the substrate material during the CMTW process. This study helped in extending the versatility of the CMT process in the welding of superalloy materials.
Key words: Cold Metal Transfer Welding, Hastelloy C-22, SS 308L, Finite element analysis, Material characterization.

1. INTRODUCTION

Welding is widely used to fabricate a variety of products in different industries. However, thin specimens of metals and alloys have a possibility of distortion when welded through traditional arc welding, so heat dissipators or other thermal protection arrangements are used to restrict the weldment distortion and warpage [1]. The combination of low voltage and low welding heat stands advantageous for thin sheet materials, and such operating conditions are available with the Cold Metal Transfer Welding (CMTW) process [2]. Another area of concern is the lower weld efficiency associated with the welding of similar and dissimilar materials; however, such a problem was also addressed during the implementation of the CMT process [3]. CMTW, referred regarded as a 'cold' process, produces substantially less heat than conventional metal inert gas/metal active gas welding. This technique operates on the principle of short-circuiting—where the electrode wire is quickly retracted through robotic actuation and electronic control—facilitating the separation and transfer of a molten droplet to the weld pool. Once the droplet separates, the arc reignites, enabling the weld zone to cool slightly before the next cycle begins. This cyclic heat regulation results in smoother weld beads and stronger joints than those produced by high-heat-input joining techniques [4, 5]. Hence, the CMTW process worked well for joining thin material specimens that were otherwise prone to warping and weld burn-through. Due to its minimal heat input, the CMTW process is ideal for welding thin sheet materials (< 10 mm), outperforming traditional gas metal arc welding (GMAW) in efficiency and preserving the metals' microstructure without sacrificing joint strength [6, 7]. As a result, thermal shielding is seldom required during CMTW. These advantages have resulted in its extensive implementation across several industries, including automotive and marine sectors.

Extensive studies have been conducted on the CMTW process for both similar and dissimilar metal weldments for a wide variety of ferrous and non-ferrous materials. Sun et al. [8] investigated the droplet transfer behavior during CMTW of Ti alloy by capturing electrical waveforms and high-speed images of the transfer process. To understand the transfer mechanism better, further analysis on the relationship among current pulses, energy distribution, droplet transfer frequency, wire feed rate, and inductance correction values was carried out. Tian et al. [9] have studied the weldability of the Ai/Al alloy by CMT technology and proposed that the initial deposition of Ti alloy is better suited for the CMT-based wire and arc additive manufactured process. Joining of thin sheet Al-Steel combination using CMT process has been investigated by Chen et al. [10] to find a suitable parametric window between wire feed speed, welding speed and arc length. For better penetration and material deposition during the CMTW process, edge preparation (preferably V-groove) also plays an important role, as reported by

several researchers [11, 12]. Li et al. [13] have investigated an innovative CMT technology for joining Al/7N01 and reported a lack of pores and defects in the weld, which was due to a lower value of heat input. Singh et al. [14] have reported a novel CMT + P weld-brazing to join AA5052 and DP780 alloy and plotted cyclograms for different wire feed rates and pulses. Experimental studies on arc length correction indicate that variations in droplet size, weld bead geometry, and mechanical properties occur when the arc length correction value ranges from -20% to +20% [15, 16, 17]. Process parameters were optimized to control bead geometry, including bead width, reinforcement height, and penetration depth. A few hybrid welding processes with CMTW have also been reported with substantial enhancement of joint performance [18, 19, 20].

Superalloys are a specialized class of high-performance materials known for their exceptional resistance to corrosion and for keeping their strength and durability even at very high temperatures. Hastelloy C-22 is a superalloy made of a specific composition of Ni, Cr, Mo and W, that is more resistant to pitting caused by chloride [21]. Most of the studies reported on Hastelloy C-22 are related to the analysis of corrosion resistance in various mediums such as 3.5% NaCl solution [22], molten alkali salts [23], $H_2SO_4/Fe_2(SO4)_3$ solution [24], hydrochloric, sulfuric and nitric acid solutions [25], sulphate solutions of low pH and low temperatures [26], H_2S at high temperature [27], etc., however, welding studies for the same alloy is not available. So, a novel attempt has been made to carry out bead-on-plate (BOP) CMTW of Hastelloy C-22 sheet and analyze the bead geometry and microstructure formation, and correlate the same with the thermal cycle obtained through finite element analysis (FEA).

Based upon the literature, the following research objectives (RO) have been pursued for the present investigation:

RO 1: To achieve a successful fusion between Hastelloy C-22 and stainless steel by the CMTW process.

RO 2: To analyze the macrostructure and microstructure of the weld bead.

RO 3: To carry out finite element modeling (FEM) analysis of the BOP CMTW of Hastelloy C-22 sheet.

2. MATERIALS AND METHODS

The CMTW setup used in the present study for BOP welding of a 1.5 mm thick Hastelloy C-22 sheet using SS 308L filler wire is shown in the fig. 1. The CMTW setup consists of (a) Fronius TransPulsSynergic 2700 power source and (b) work table. The specification of the Fronius TransPulsSynergic 2700 power source is mentioned in Table 1. The welding torch is controlled by the robotic arm, and the BOP welding was carried out on the Hastelloy C-22 sheet sample clamped to the work table using fixtures (shown in the fig. 1).

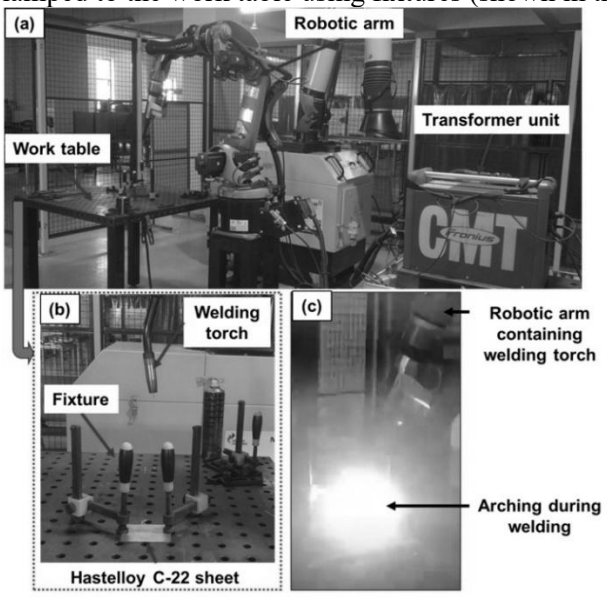

Fig. 1. CMTW setup used in present study for BOP welding of Hastelloy C-22 sheets.

Table 1. Specifications of Fronius TransPuls Synergic 2700 CMT welding machine

Control parameter	Value
Welding voltage	10 – 34 V
Welding current range	3 – 270 A
Wire feed speed	0.5 – 22 m/min
Maximum shielding gas pressure	7 bar

Table 2. Composition (wt.%) of as-received Hastelloy C-22 sheet

Ni	Cr	Mo	Fe	W	Co	Cu	Mn	V	Si	C
55.70	20.20	12.50	4.50	4.50	0.30	0.90	0.80	0.39	0.20	0.01

Table 3. Composition (wt.%) of SS 308L filler wire

Fe	Cr	Ni	Mn	Si	P	S	C
70.61	18.55	7.85	2.30	0.49	0.07	0.08	0.05

Table 4. Information related to BOP CMTW of Hastelloy C-22 sheet

CMT machine manufacturer and model	Fronius TransPuls Synergic 2700
Applied voltage	12 V
Welding current	70 A
Welding speed	200 mm/min
Shielding gas	Argon (99.99 %)
Shielding gas flow rate	16 l/min
Filler wire	SS 308L
Filler wire thickness	1.2 mm
Extension length of filler wire	10 mm
Mode of voltage application	Synergic
Mode of current application	Synergic

```
DLFUX Program User Subroutine Interface
SUBROUTINE DFLUX(FLUX,SOL,KSTEP,KINC,TIME,NOEL,NPT,COORDS,JLTYP,TEMP,PRESS,SNAME)
INCLUDE 'ABA_PARAM.INC'
DIMENSION FLUX(2),TIME(2),COORDS(3)
CHARACTER*80 SNAME
P(W)
v(m/s)
h(m)
r_αz(m)
α_z(Constant)
r_0(m)
r_z(m)
r=SQRT((COORDS(1))^2+(COORDS(2)-v*TIME(2))^2)
r_z=r_0-((r_0-r_αz)z/(α_z h))
FLUX(1)=(P*exp[(1-(r^2/r_z^2))(1-(z/h))])/(π*(r_αz^2(1-(2/3)α_z))*h)
RETURN
END
```

Fig. 2. Program used to perform FEM.

The chemical composition of the supplied base metal (Hastelloy C-22) and the filler wire (SS 308L) preferred for the present investigation are given in Tables 2 and 3, respectively. In advance of the BOP experiment, the 1.5 mm thick Hastelloy C-22 was properly cleaned in the region of bead deposition to avoid any surface contamination. The CMTW machine make and model, list of parameters, and operating conditions are shown in Table 4. A JEOL JSM-IT800 field emission scanning electron microscope (SEM) coupled with the EDAX AMETEK detector was employed to study the microstructural features and energy-dispersive X-ray spectroscopy (EDS) analysis of the weldment. X-ray diffraction (XRD) scanning of the weld bead was carried out using a Bruker D8 Advance X-ray Diffractometer with copper as the target material and at a wavelength of 1.54 Å for X-ray emission. The continuous 2θ scan conditions of the weld bead include (a) range: 20° to 120°, (b) step size = 0.02°, and (c) count time = 1 s per step. In the present CMTW process, the weld bead was formed due to the simultaneous action of melting of the Hastelloy C-22 sheet and deposition of SS 308L filler wire (during the short-circuiting mode of metal transfer). Hence, there exists a possibility of intermixing between materials (Hastelloy C-22 sheet and SS 308L filler wire) in the weld zone. A study related to the thermal cycle would help understand the microstructure and phase formed in certain isotherms of the temperature distribution in the CMTW process. ABAQUS FEA software was used to develop a model and replicate the shape of the cross-sectional image of the weld bead for the present BOP CMTW process. The entire process of the FE simulation included: part development, property assignment, assembly stage, step definition, interaction definition, load allocation, part meshing, job submission, and result visualization. Fig. 2 shows the program used to perform FEM in the present study.

3. RESULTS AND DISCUSSION

3.1. Analysis of bead geometry

After the BOP CMTW process, the sample was precisely cut along its cross-section, subjected to etching in an acidic solution that comprised 15 ml of HCl, 10 ml of HNO_3, and 10 ml of $C_2H_4O_2$, and examined under the optical microscope. The weld bead cross-sectional image for BOP CMTW at a parametric combination of 12 V − 70 A − 200 mm/min is presented in figure 3(a).

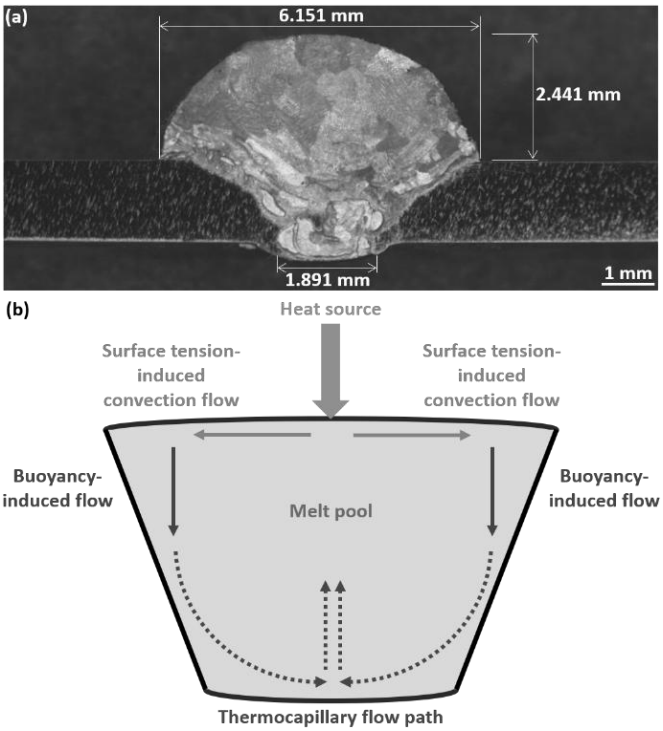

Fig. 3. (a) Cross-sectional image of weld bead for BOP CMTW at 12 V − 70 A − 200 mm/min. (b) Schematic diagram showing probable forces acting in the melt pool.

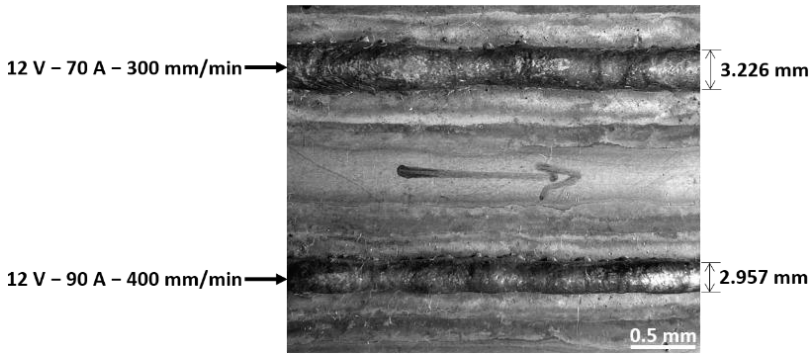

Fig. 4. BOP CMTW carried out at different parameters.

The weld bead cross-section resembles an oval countersunk head type shape (fig. 3(a)) and could have formed due to the conduction mode of welding [28]. Fig. 3(b) shows a schematic diagram illustrating the different forces probably acting in the melt pool. Marangoni convection, also known as thermocapillary flow [29], may have influenced the morphology of the weld bead observed in this study. The surface tension-induced convective flow (STICF) usually moves the hot and molten metal away from the center of the weld and toward a cooler location [30]. This action provides the width or increases the width of the weld bead at the top. The buoyancy force-induced flow (BFIF), at the other end, pulls the colder fluid to the bottom. This process makes the weld bead deeper. Consequently, the combined effects of STICF and BFIF regulate the flow of molten metal within the weld bead, which in turn determines the shape of the weld bead when the melt pool solidifies. The dashed arrows in the figure 3(b) shows the thermocapillary flow path, the action of which could have resulted in a probable path of fluid flow subsurface, i.e., along the boundary wall and at the bottom of the weld bead. The weld bead cross-sectional image (fig. 3(a)) shows a fully-penetrated and defect-free weld with no significant sheet deformation or

spatter. Experiments conducted with different combinations of welding current and speed (fig. 4) also demonstrated the absence of spatter or any other sheet deformity.

3.2. FEM and Metallography analysis of BOP CMTW of Hastelloy C-22 sheet

For the FE simulation, the weld bead cross-sectional geometry for the current study was modeled by implementing a modified mobile three-dimensional (3D) volumetric heat source. Equations 1 and 2 [31] represent the volumetric heat source Q (r, z) used for FE simulation in the present study.

$$\boldsymbol{Q(r,z) = \frac{P \times exp\left[\left(1-\frac{r^2}{r_z^2}\right)\left(1-\frac{z}{h}\right)\right]}{\pi \times \left(r_{\alpha z}^2\left(1-\frac{2}{3}\alpha_z\right)\right) \times h}} \quad (1)$$

where:

r = Heat source instantaneous radius = $\sqrt{x^2 + y^2}$;
z = Instantaneous depth with respect to the part model;
P = Heat source power (absorbed) = 400 W;
r_z = Heat source radius along the depth;
h = Heat source effective (or total) penetration depth = 0.2 mm;
$r_{\alpha z}$ = Heat source radius at the depth 'z' with respect to the part model = $\alpha_z h$, where $\alpha_z \in [0; 1] \approx 0.9$ mm;
r_0 = Heat source radius incident on the surface of the part model = 1.4 mm;
v = Heat source scan speed = 200 mm/min.

$$\mathbf{r_z = r_0 - \left((r_0 - r_{\alpha z})\frac{z}{\alpha_z h}\right)} \quad (2)$$

The thermophysical properties for the Hastelloy C-22 part model, such as density, latent heat, thermal conductivity, expansion coefficient, solidus temperature, liquidus temperature, and specific heat, were cited from the reported literature [21, 32], followed by the assumption of linear interpolation till the temperature of 2500 °C. Figure 5 shows the configuration of the part model for analysis through FE simulation, along with the dimensions, heat source movement (scan) direction, heat transfer conditions, and symmetric plane.

The simulation of the part model includes the transient heat transfer step of (a) heating cycle = '6 s' and (b) cooling cycle = '7 s'. Other parameters include: (1) geometric nonlinearity = 'off', (2) 'automatic' step increment, (3) maximum number of increments = '10^7', and (4) solution method = Full Newton approach. The values of surface convection (= 10 W/m^{2}K [33]) and radiation (0.9 (at 901 °C) [34]) were assigned to the part model in the interaction step. The details of the uniform meshing of the part model are mentioned in the fig. 5 caption. The flux distribution in the volume of the part model was set to 'user-defined', so that FE analysis could be simulated through a coded 'DFLUX' file (fig. 2) [35]. The analysis of the part model was done through ABAQUS/Standard to predict the nodal temperature 'NT' distribution. The heat transfer equation, considered for analysis in the present study, was transient and is shown by equation 3 [36].

$$\underbrace{\mathbf{Q}}_{\substack{\textit{Net heat}\\ \textit{transfer}}} = \underbrace{\mathbf{K}\left(\frac{\partial \mathbf{T}}{\partial \mathbf{n}}\right)}_{\substack{\textit{Conduction}\\ \textit{transfer}}} + \underbrace{\mathbf{h}(\mathbf{T} - \mathbf{T_o})}_{\substack{\textit{Convection}\\ \textit{transhfer}}} + \underbrace{\boldsymbol{\sigma\varepsilon}\left(\mathbf{T^4} - \mathbf{T_o^4}\right)}_{\substack{\textit{Radiation}\\ \textit{transfer}}} \quad (3)$$

where: Q = Volumetric heat flux of a Gaussian distribution nature; K = Materials' thermal conductivity; T = Temperature at a given coordinate location; n = Direction orthogonal to the surface; h = Convective heat transfer coefficient; T_o = Temperature of the ambient; σ = Stefan–Boltzmann constant; ε = Materials' emissivity.

Fig. 6(a) presents the combined image of the experimental weld bead geometry alongside the finite-element generated weld bead, and a reasonable consistency was observed between the two. The isotherm depicted in the fig. 6(a) reveals that the heat could have transferred via conduction mode during the CMTW process, and the findings were further supported by the heat flux vector (HFL) as presented in Figure 7. The HFL shows how much heat is flowing and in what direction it is moving during the thermal transfer process. The conduction mode of heat transfer is usually represented by a semi-circular-shaped isotherm generation and 3D heat propagation, and a similar process was observed in the present study.

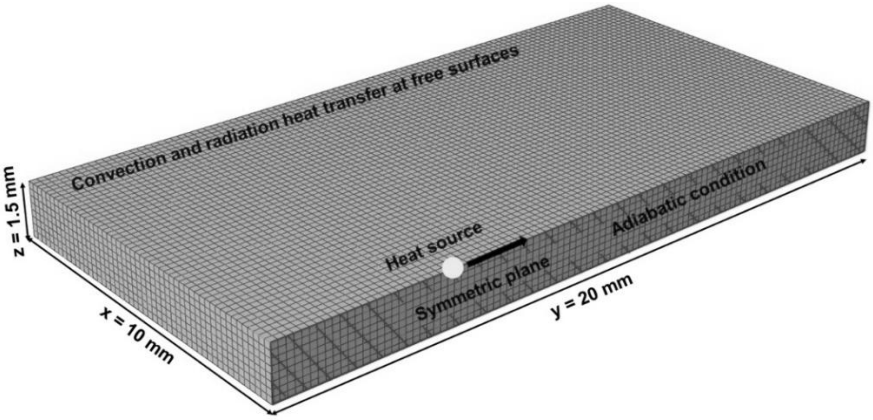

Fig. 5. Part configuration used for FE simulation. Mesh information: element type = hexahedral DC3D8, linear elements = 40000, nodes = 46359.

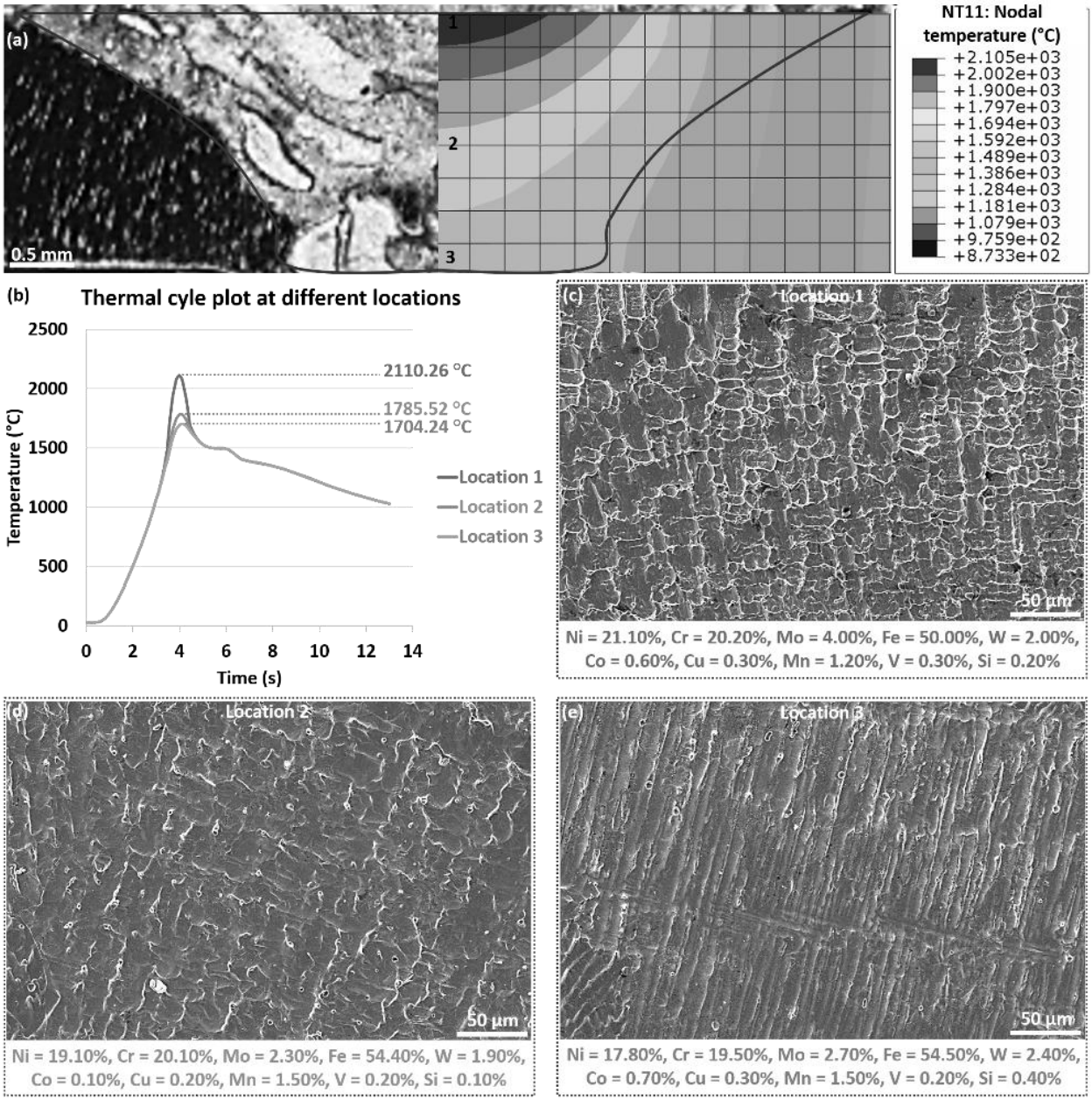

Fig. 6. (a) Merged image of experimental weld bead and FE simulated weld bead. NT11 denotes Nodal temperature (°C). (b) Thermal cycle plot at different locations 1, 2, 3 in the simulated weld bead. Microstructure and EDS analysis at (c) location 1, (d) location 2, and (e) location 3.

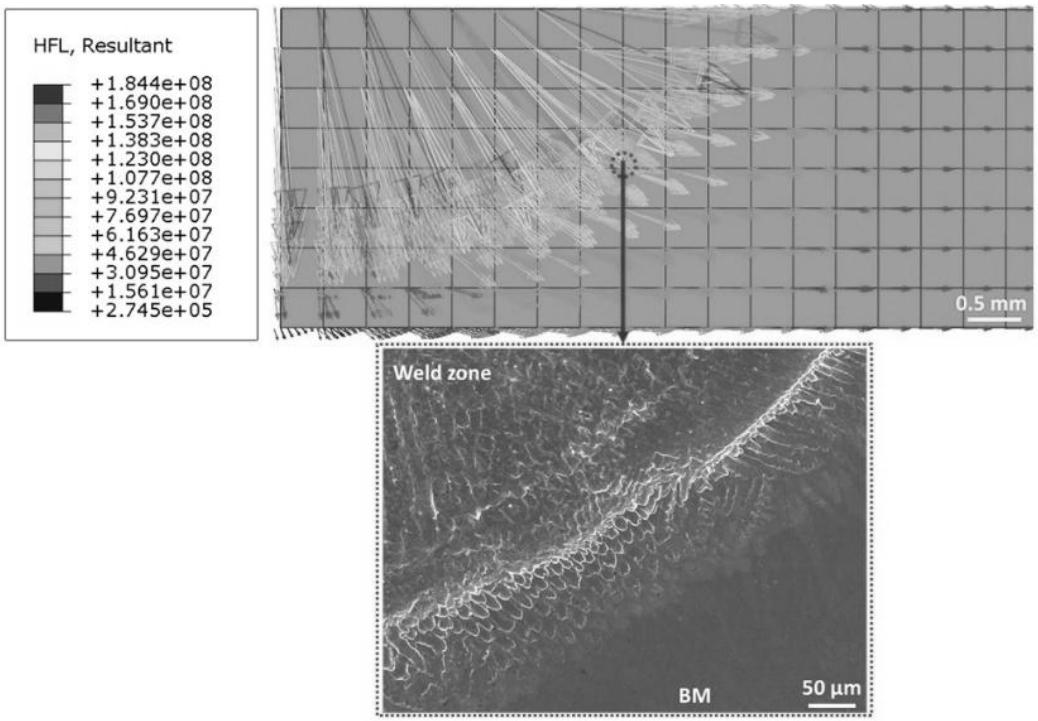

Fig. 7. HFL vector showing magnitude (in W/m^2) and direction of heat flow from different nodes of FE simulated weld zone. Magnified view of interface between weld zone and BM is shown corresponding to location in FE simulated weld zone.

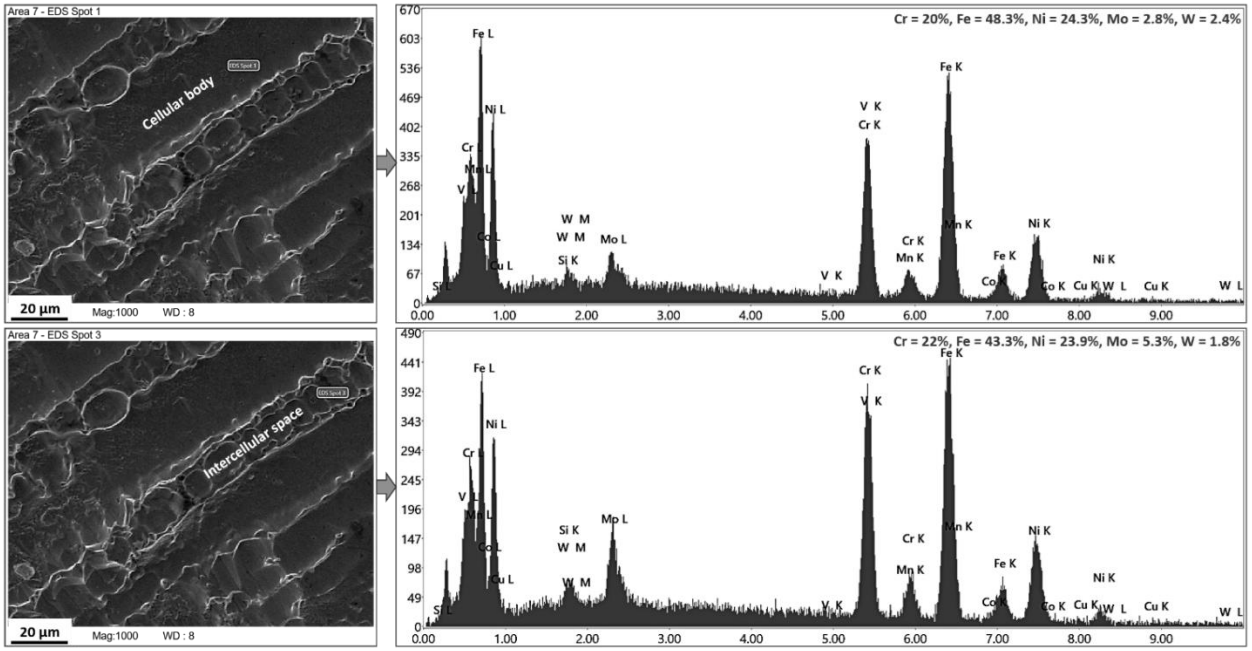

Fig. 8. Magnified view of weld zone showing cellular body and intercellular space along with EDS analysis.

An enhanced view (fig. 7) of a specific area in the FE-simulated weld zone illustrated the transition zone (interface) between the weld zone and the base metal (BM), and is synonymous with the HFL vector representation. It could be suggested from the fig. 6(a) that the weld zone contains various isotherms where different microstructures and phases might be formed. Hence, a correlation between the thermal cycle and the phase formation has been further analyzed. Fig. 6(b) shows the thermal cycle, i.e., temperature–time plot, at three different locations (nodes) 1, 2, 3 obtained through FEA. The peak temperatures for location 1, location 2 and location 3 were observed to be 2110.26 ˚C, 1785.52 ˚C and 1704.24 ˚C, respectively. The microstructures corresponding to locations (1, 2, 3) in the weld bead are shown in the fig. 6(c, d, e), respectively. It could be seen that equiaxed structures of varying morphologies were formed in the three locations, and their respective spot EDS shows a similar composition of constituent elements with minor variations, except for Ni and Fe. The

concentration of Ni has decreased by 15.63% from 21.10 wt.% to 17.80 wt.%, while that of Fe has increased by 9% from 50.00 wt.% to 54.50 wt.%. This varying distribution of constituent elements has occurred due to their location in different isotherm regions, which consecutively affected their diffusion rate (both in solid and liquid state) during the weld solidification. The cooling rate of the melt pool was found to be 50 °C/s from the temperature–time curve (fig. 6(b)) when the solidification of the melt pool was considered within the liquidus temperature of SS 308L (= 1420 °C [37]) and the solidus temperature of Hastelloy C-22 (= 1399 °C [21]). Such a magnitude of cooling rate might have also played an important role in the variation of elemental concentration observed at different locations within the weld bead.

Fig. 8 presents the magnified view of the weld zone showing the formation of the cellular body and intercellular space. In the present study, apparent microsegregation of major constituent elements (Cr, Fe, Ni, Mo, W) from the cellular body to the intercellular space was determined via wt.% data collected through EDS analysis (fig. 8). The segregation ratio (SR) [38], i.e., ratio of (element wt.%)$_{\text{intercellular space}}$ to (element wt.%)$_{\text{cellular body}}$, was calculated. An SR value more than 1 indicates the segregation of the element from the cellular body to the intercellular space during weld zone solidification. The calculated SR values of Fe (= 0.89), Ni (= 0.98) and W (= 0.75) show no segregation characteristics. On the other hand, the SR value of Mo (= 1.89) and Cr (= 1.1) show segregation to the intercellular space; however, the segregation of Cr was less significant than Mo. The atomic size difference (approx. −9%) followed by limited high temperature solubility (approx. 34%) of Mo in reference to Ni [39] could have resulted in Mo segregation in the present study.

3.3. Crystallographic analysis of BOP CMTW of Hastelloy C-22 sheet

Five major peaks (between 50° to 120°) were detected during the scanning, and Figure 9 shows the phases identified through the XRD analysis. It could be observed from Figure 9 that out of five peaks, the first three peaks (57.601°, 57.880°, and 97.035°) consist of Fe-based phases (Fe-W-Co-Mo-C, Fe-Si-Mo-Co, and Fe-W-Si) formed in the weld bead, which could probably be due to filler materials' contribution of Fe. The phases detected in the last two peak positions (97.772° and 118.445°) include complex phases of Ni-Cr-Fe-W-Co and Cr-Fe-Ni-Si-Mo-C, which may be due to the BM of Hastelloy C-22 and SS 308L filler wire. As estimated earlier about the possibility of 'intermixing of materials of Hastelloy C-22 sheet and SS 308L filler wire in the weld zone', hence, from the XRD analysis, it may be possible to infer that indeed an intermixing of elements (Ni, Cr, Mo, Fe, Co, W, C, Si and other constituent) from both the materials have occurred and this has led to the formation of complex phases. To further support this inference, an EDS area scanning of the weld bead area was conducted to analyze the relative distribution of elements within the weld bead, as indicated in Figure 10.

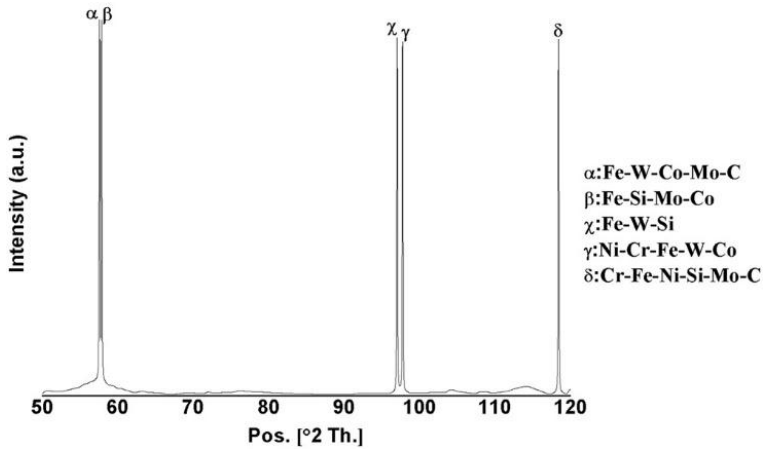

Fig. 9. XRD graph of BOP CMTW of Hastelloy C-22 sheet.

Fig. 10 demonstrates that all of the elements (Ni, Cr, Mo, Fe, W, Co, Cu, Mn, V, Si) are evenly distributed across the weld zone. The weld bead revealed a higher concentration of the Fe element due to the deposition of filler material during the CMT process. The concentration of Ni was observed to be higher at the BM, and at the same time, Ni was uniformly distributed in the weld zone. Mo also follows a similar distribution pattern to that of Ni. The other constituent elements like Cr, W, Co, Cu, Mn, V and Si showed uniform distribution throughout the mapped area. Overall, the weld bead consists of elements from both the materials with uniform distribution throughout, which might have been possible due to the low heat input and high solidification rate features of the CMT process.

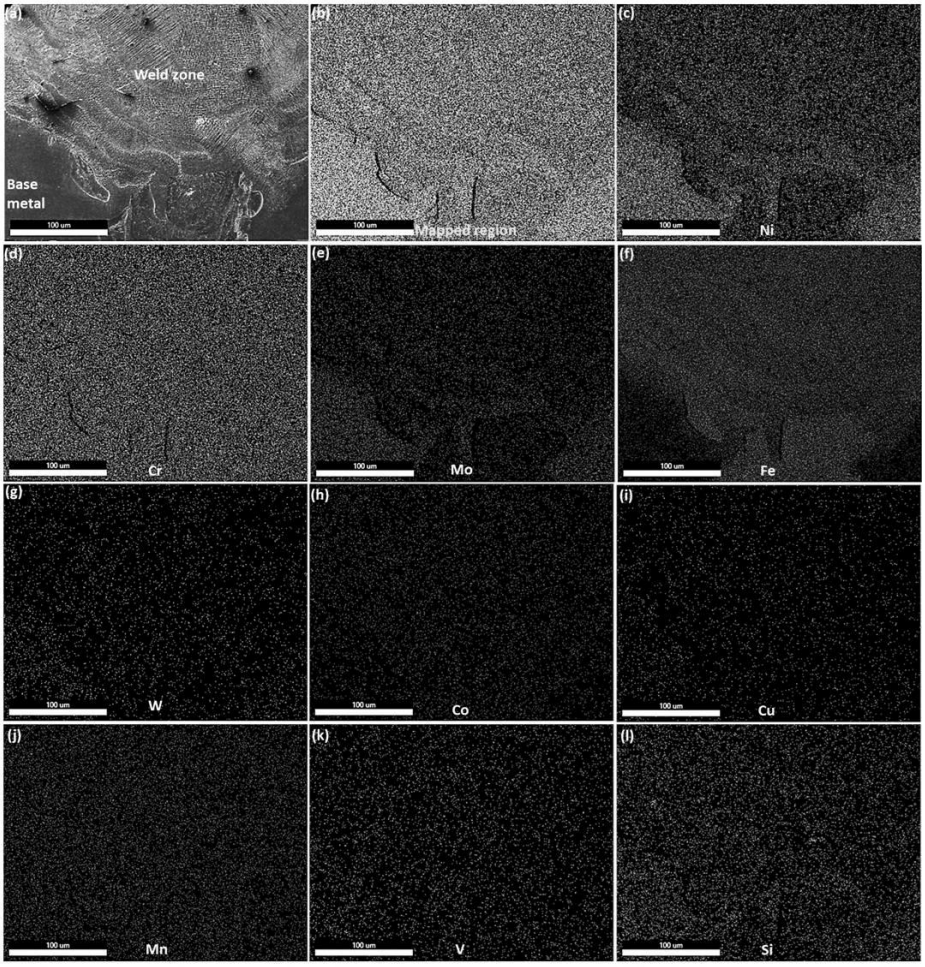

Fig. 10. EDS map analysis of BOP weld bead.

4. CONCLUSIONS

The following are the conclusions obtained from the present study i.e., experimental analysis of the BOP CMTW Hastelloy C-22 sheet:

BOP CMTW of Hastelloy C-22 sheet has been done successfully with SS 308L filler wire. An oval countersunk head-type shaped weld bead was observed to be formed.

A 3D volumetric heat source was successfully implemented for FEM analysis of the BOP CMTW of Hastelloy C-22 sheet, and the thermal cycle was obtained for the entire welding process.

The SEM and EDS analysis show the formation of equiaxed microstructure with different morphology and minorly varying chemical compositions for Ni and Fe at different locations within the weld bead.

The cooling rate of the melt pool was found to be 50 $^{\circ}$C/s, which could have been a reason for varying elemental concentration at different zones within the weld bead.

The analysis of the HFL vector showed the occurrence of a 3D heat flow distribution for the weld bead formation in the present CMTW process.

EDS map analysis shows a higher concentration of Fe in the weld bead, and the same is replicated by the Fe-based phases formed as detected through XRD analysis.

The implementation of the 'synergic' mode for the CMTW process proved beneficial in terms of efficient control of weld parameters and appreciable intermixing of dissimilar material of filler and base material.

Author contributions: All authors contributed to the study conception and design. Data curation, investigation, methodology, validation, and initial draft writing were performed by Anish K Raj. Conceptualization, resources, supervision, visualization, review and editing were performed by Bikash Ranjan Moharana. Data curation, supervision, review and editing were performed by Kalinga Simant Bal. Supervision, review and editing were performed by Shaik Mozammil. All authors have read and agreed to the published version of the manuscript.

Funding source: The research received no specific grant from any funding agency.

Conflicts of interest: There is no conflict of interest

Acknowledgements: The authors are grateful to Dr. Sushovan Basak, C. V. Raman Global University for providing support during the CMT welding experiment. The authors want to extend their sincere thanks to Mr. Anitesh Kumar Singh, Indian Institute of Technology Kharagpur, for extending his needful support in the ABAQUS software. The authors want to thank the Technical Team of Central Laboratory for Instrumentation and Facilitation (CLIF), University of Kerala, for extending instrumentation support of CLIF for the XRD analysis of the sample. The authors also want to thank Er. Shubhra Bajpai, Principal Scientist, and Mr. Alok Kumar Prusty of Council of Scientific & Industrial Research - Institute of Minerals & Materials Technology (CSIR-IMMT), Bhubaneswar, for extending instrumental support of Field Emission SEM and EDS for sample analysis. The authors are grateful to all the faculty members, technical staff, and research scholars of the National Institute of Technology Raipur for extending their support in carrying out this study.

5. REFERENCES

[1]. Tsai, C.L., Park, S.C., Cheng, W.T., (1999). *Welding distortion of a thin-plate panel structure*. Welding journal-New York, 78, pp.156-s.
https://www.ccctc.k12.oh.us/Downloads/Article%20Welding%20Distortion%20of%20Thin%20Plate.pdf. (Accessed: 01 December 2025).
[2]. Cong, B., Ouyang, R., Qi, B., Ding, J., (2016). *Influence of cold metal transfer process and its heat input on weld bead geometry and porosity of aluminum-copper alloy welds*. Rare Metal Materials and Engineering, 45(3), 606-611, https://doi.org/10.1016/S1875-5372(16)30080-7.
[3]. Selvi, S., Vishvaksenan, A., Rajasekar, E., (2018). *Cold metal transfer (CMT) technology-An overview*. Defence technology, 14(1), 28-44, https://doi.org/10.1016/j.dt.2017.08.002.
[4]. Hu, S., Zhang, H., Wang, Z., Liang, Y., Liu, Y., (2016). *The arc characteristics of cold metal transfer welding with AZ31 magnesium alloy wire*. Journal of Manufacturing Processes, 24, 298-306, https://doi.org/10.1016/j.jmapro.2016.10.001.
[5]. Balasubramanian, M., Choudary, M.V., Nagaraja, A., Sai, K.O.C., (2020). *Cold metal transfer process–a review*. Materials Today: Proceedings, 33, 543-549, https://doi.org/10.1016/j.matpr.2020.05.225.
[6]. Pickin, C.G., Young, K., (2006). *Evaluation of cold metal transfer (CMT) process for welding aluminium alloy*. Science and Technology of Welding and Joining, 11(5), 583-585, https://doi.org/10.1179/174329306X120886.
[7]. Ahsan, M.R., Kim, Y.R., Kim, C.H., Kim, J.W., Ashiri, R., Park, Y.D., (2016). *Porosity formation mechanisms in cold metal transfer (CMT) gas metal arc welding (GMAW) of zinc coated steels*. Science and Technology of Welding and Joining, 21(3), 209-215, https://doi.org/10.1179/1362171815Y.0000000084.
[8]. Sun, Z., Lv, Y., Xu, B., Liu, Y., Lin, J., Wang, K., (2015). *Investigation of droplet transfer behaviours in cold metal transfer (CMT) process on welding Ti-6Al-4V alloy*. The International Journal of Advanced Manufacturing Technology, 80, 2007-2014, https://doi.org/10.1007/s00170-015-7197-9.
[9]. Tian, Y., Shen, J., Hu, S., Gou, J., Kannatey-Asibu, E., (2019). *Wire and arc additive manufactured Ti–6Al–4V/Al–6.25 Cu dissimilar alloys by CMT-welding: effect of deposition order on reaction layer*. Science and Technology of Welding and Joining, 25(1), 73-80, https://doi.org/10.1080/13621718.2019.1629379.
[10]. Chen, C., Gao, C., Xing, Y., (2018). *Investigations on the dissimilar metal joints capability between aluminum alloy and steel under CMT welding*. In MATEC Web of Conferences, Vol. 228, pp. 04007. EDP Sciences, https://doi.org/10.1051/matecconf/201822804007.
[11]. Li, G., Song, J., Lu, X., Zhu, X., Xu, S., Guo, Y., (2020). *Investigation on microstructure and mechanical properties of Al/Cu butt joints by CMT method in asymmetrical V-groove configuration*. Metallurgical Research & Technology, 117(3), pp.303, https://doi.org/10.1051/metal/2020028.
[12]. Mou, G., Hua, X., Wu, D., Huang, Y., Lin, W., Xu, P., (2019). *Microstructure and mechanical properties of cold metal transfer welding-brazing of titanium alloy (TC4) to stainless steel (304L) using V-shaped groove joints*. Journal of Materials Processing Technology, 266, 696-706, https://doi.org/10.1016/j.jmatprotec.2018.09.019.
[13]. Li, J., Shen, J., Hu, S., Liang, Y., Wang, Q., (2019). *Microstructure and mechanical properties of 6061/7N01 CMT+ P joints*. Journal of Materials Processing Technology, 264, 134-144, https://doi.org/10.1016/j.jmatprotec.2018.09.011.
[14]. Singh, J., Arora, K.S., Shukla, D.K., 2020. *Lap weld-brazing of aluminium to steel using novel cold metal transfer process.* Journal of Materials Processing Technology, 283, pp.116728, https://doi.org/10.1016/j.jmatprotec.2020.116728.
[15]. Raj, D., Singari, R.M., Vipin, M., (2022). *Study and analyses of arc length correction and mechanical properties on weld bead geometry for AA6061T6 by CMT process*. Materials Today: Proceedings, 56, 3475-3483, https://doi.org/10.1016/j.matpr.2021.11.122.

[16]. Cai, M., Wu, C., Gao, X., (2018). *The influence of arc length correction on welding in cmt welding*. In IOP Conference Series: Earth and Environmental Science, 170(4), pp. 042106). IOP Publishing House, doi :10.1088/1755-1315/170/4/042106.
[17]. Kannan, A.R., Shanmugam, N.S., Naveenkumar, S., (2019). *Effect of arc length correction on weld bead geometry and mechanical properties of AISI 316L weldments by cold metal transfer (CMT) process*. Materials Today: Proceedings, 18, 3916-3921, https://doi.org/10.1016/j.matpr.2019.07.331.
[18]. Rajendran, C., Sonar, T., Ivanov, M., Sandeep, C., Shanthi, C., Gurajala, N. K., Xu, J., (2024). *Enhancing tensile properties of pulsed CMT–MIG welded high strength AA2014-T6 alloy joints: effect of post weld heat treatment*. International Journal of Lightweight Materials and Manufacture, 7(2), 344-352, https://doi.org/10.1016/j.ijlmm.2023.10.004.
[19]. Su, J., Hu, M., Li, Z., Wang, X., Guo, Q., Luo, Z., (2025). *Substantial enhancement in thin-walled stainless steel fillet weld joint performance via high-speed laser-CMT hybrid welding*. Thin-Walled Structures, 214, p.113320, https://doi.org/10.1016/j.tws.2025.113320.
[20]. Khajuria, A., Misra, A., Shiva, S., (2024). *The influence of CMT-MAG and MAG welding-processes on microstructure and mechanical behaviour of C-Mn E410 structural-steels*. International Journal of Structural Integrity, 15(2), 322-342, https://doi.org/10.1108/IJSI-12-2023-0141.
[21]. Haynes International, (2023). *HASTELLOY®C-22®alloy*. Available at: https://haynesintl.com/wp-content/uploads/2024/08/c-22-brochure.pdf. (Accessed: 01 December 2025).
[22]. Chen, L., Bai, S.L., (2018). *The anti-corrosion behavior under multi-factor impingement of Hastelloy C22 coating prepared by multilayer laser cladding*. Applied Surface Science, 437, 1-12, https://doi.org/10.1016/j.apsusc.2017.12.108.
[23]. Kassim, S.A., Thor, J.A., Seman, A.A., Abdullah, T.K., (2020). *High temperature corrosion of Hastelloy C22 in molten alkali salts: The effect of pre-oxidation treatment*. Corrosion Science, 173, p.108761, https://doi.org/10.1016/j.corsci.2020.108761.
[24]. Wang, Q.Y., Zhang, X.S., Zheng, H.B., Liu, T.Y., Dong, L.J., Zhang, J., Xi, Y.C., Zeng, D.Z., Lin, Y.H., Luo, H., (2023). *Intergranular corrosion mechanism of sub-grain in laser additive manufactured Hastelloy C22 induced by heat treatment*. Applied Surface Science, 608, pp.155140, https://doi.org/10.1016/j.apsusc.2022.155140.
[25]. Wang, Q.Y., Bai, S.L., Liu, Z.D., (2014). *Corrosion behavior of Hastelloy C22 coating produced by laser cladding in static and cavitation acid solution. Transactions of Nonferrous Metals Society of China*, 24(5), 1610-1618, https://doi.org/10.1016/S1003-6326(14)63232-5.
[26]. Bellanger, G., Rameau, J.J., (1996). *Behaviour of Hastelloy C22 steel in sulphate solutions at pH 3 and low temperatures*. Journal of materials science, 31, 2097-2108, https://doi.org/10.1007/BF00356632.
[27]. Liu, Z., Liu, C., Gao, Y., Zheng, C., (2020). *High temperature corrosion behaviors of 20G steel, hastelloy C22 alloy and C22 laser coating under reducing atmosphere with H_2S*. Coatings, 10(7), pp.617, https://doi.org/10.3390/coatings10070617.
[28]. Bal, K.S., Dutta Majumdar, J., Roy Choudhury, A., (2019). *Effect of electron beam accelerating voltage on the melt zone area, secondary-dendrite arm spacing and fusion line microstructure of bead-on-plate welded Hastelloy C-276 sheet*. Optik, 183, 355-366, https://doi.org/10.1016/j.ijleo.2019.02.084.
[29]. Das, D., Bal, K.S., Pratihar, D.K., Roy, G.G., (20210. *Correlating the weld-bead's 'macro-, micro-features' with the weld-pool's 'fluid flow'for electron beam welded SS 201 plates*. International Journal of Mechanical Sciences, 210, pp.106734, https://doi.org/10.1016/j.ijmecsci.2021.106734.
[30]. Kou, S., (2003). Welding metallurgy, New Jersey, USA, 431(446), 223-225.
[31]. Piekarska, W., Kubiak, M., (2012). *Theoretical investigations into heat transfer in laser-welded steel sheets. Journal of thermal analysis and calorimetry*, 110(1), 159-166, https://doi.org/10.1007/s10973-012-2486-0.
[32]. AZoNetwork, (2023). *AZOMATERIALS: Nickel Chrome Alloys - Properties and Applications*. https://www.azom.com/properties.aspx?ArticleID=916. (Accessed: 01 December 2025).
[33]. Kosky, P., Balmer, R., Keat, W.D. and Wise, G., 2021. Exploring Engineering: An Introduction to Engineering and Design. Academic Press, pp. 322, London.
[34]. Gadek, T., Nowacki, L., Drenger, T., (2014). *Hot spinning of the Hastelloy C-276 alloy using a high-power diode laser*. Obrob Plast, 4, 287-299.
[35]. Abaqus, (2016). *1.1.3 DFLUX User subroutine to define nonuniform distributed flux in a heat transfer or mass diffusion analysis,* available at: http://130.149.89.49:2080/v2016/books/sub/default.htm?startat=ch01s01asb03.html. (Accessed: 01 December 2025).

[36]. Baruah, M., Bag, S., (2017). *Influence of pulsation in thermo-mechanical analysis on laser micro-welding of Ti6Al4V alloy*. Optics & Laser Technology, 90, 40-51, https://doi.org/10.1016/j.optlastec.2016.11.006.
[37]. MakeItFrom.com, (2020). *AISI 308L (S30880, ER308) Stainless Steel.* https://www.makeitfrom.com/material-properties/AISI-308L-S30880-ER308-Stainless-Steel, accessed: 01 December 2025.
[38]. Zhang, Y., Li, J., (2012). *Characterization of the microstructure evolution and microsegregation in a Ni-based superalloy under super-high thermal gradient directional solidification*. Materials Transactions, 53(11), 1910-1914, https://doi.org/10.2320/matertrans.M2012173.
[39]. Lippold, J.C., Kiser, S.D., DuPont, J.N., (2011). *Welding metallurgy and weldability of nickel-base alloys*. John Wiley & Sons, pp. 17, New Jersey.

Received: August 27th, 2025 / Accepted: December 5th, 2025 / Paper available online: December 20th, 2025